Early Detection of Amyloidopathy in Alzheimer's Mice by Hyperspectral Endoscopy

Swati S. More,[1] James M. Beach,[2] and Robert Vince[1]

[1]Center for Drug Design, Academic Health Center, University of Minnesota, Minneapolis, Minnesota, United States
[2]CytoViva, Inc., Auburn, Alabama, United States

Correspondence: Robert Vince, Center for Drug Design, 308 Harvard Street SE, 8-123A WDH, Minneapolis, MN 55455, USA; vince001@umn.edu.

Submitted: June 2, 2015
Accepted: May 4, 2016

Citation: More SS, Beach JM, Vince R. Early detection of amyloidopathy in Alzheimer's mice by hyperspectral endoscopy. *Invest Ophthalmol Vis Sci*. 2016;57:3231–3238. DOI:10.1167/iovs.15-17406

Purpose. To describe a spectral imaging system for small animal studies based on noninvasive endoscopy of the retina, and to present time-resolved spectral changes from live Alzheimer's mice prior to cognitive decline, corroborating our previous in vitro findings.

Methods. Topical endoscope fundus imaging was modified to use a machine vision camera and tunable wavelength system for acquiring monochromatic images across the visible to near-infrared spectral range. Alzheimer's APP/PS1 mice and age-matched, wild-type mice were imaged monthly from months 3 through 8 to assess changes in the fundus reflection spectrum. Optical changes were fit to Rayleigh light scatter models as measures of amyloid aggregation.

Results. Good quality spectral images of the central retina were obtained. Short-wavelength reflectance from Alzheimer's mice retinae showed significant reduction over time compared to wild-type mice. Optical changes were consistent with an increase in Rayleigh light scattering in neural retina due to soluble $A\beta_{1-42}$ aggregates. The changes in light scatter showed a monotonic increase in soluble amyloid aggregates over a 6-month period, with significant build up occurring at 7 months.

Conclusions. Hyperspectral imaging technique can be brought inexpensively to the study of retinal changes caused by Alzheimer's disease progression in live small animals. A similar previous finding of reduction in the light reflection over a range of wavelengths in isolated Alzheimer's mice retinae, was reproducible in the living Alzheimer's mice. The technique presented here has a potential for development as an early Alzheimer's retinal diagnostic test in humans, which will support the treatment outcome.

Keywords: Alzheimer's, hyperspectral, retina, endoscopy

Alzheimer's disease (AD) is a debilitating neurodegenerative disorder whose socioeconomic burden is estimated as 14 million Americans aged older than 65 years by 2050.[1] A pathognomonic indicator of this protein folding disorder is the deposition of amyloid plaques in synapses and around neuronal cells. A second pathognome is neurofibrillary tangles of hyperphosphorylated τ protein.[2] The disease leads to net loss of brain weight and volume, which can be ascribed to generalized loss of neuronal processes. The cerebral cortex and hippocampus are particularly affected.[3]

No clinical diagnostics currently exist for detecting AD prior to amyloidopathy or mild cognitive impairment. Confirmation of AD is possible only during postmortem autopsy. Currently, diagnosis of "probable" AD is possible only when the condition has progressed, and considerable irreversible neurological damage has already occurred. By the stage at which overt plaques are visible using positron emission tomography (PET) imaging,[4] cognition is already impaired. Assessment of risk for AD at an earlier stage would open a window of opportunity for therapeutic possibilities that harbor the promise of retarding or even halting the disease progression. Such an assessment would undoubtedly assist in the development of new interventions aimed at preventing or delaying the AD progression. In recent years, there has been much progress in the field of AD diagnostics and biomarker identification, including genetic, blood biomarkers, cerebrospinal fluid proteomics, and neuroimaging. Development of AD is influenced by the "risk" genes that increase the bearer's likelihood of developing AD (e.g., through apolipoprotein E–ε4 dysfunctions[5]) and the "deterministic" genes that directly generate known pathognomones such as mutant presenilin 1 and 2.[6] A panel of possible plasma biomarkers for AD has been reported.[7] Analyses of cerebrospinal fluid (CSF) has provided a potentially utile source of reliable AD biomarkers (e.g., CSF titers of amyloid $A\beta_{1-42}$, phosphorylated and total τ-peptides that have shown marked correlation with AD progression).[8,9] In brain tissue, Aβ plaques have been imaged in Alzheimer's patients using PET with ^{11}[C]-PiB and ^{18}[F]-radiolabeled ligands.[10,11] Techniques such as PET imaging can help to identify AD, but the sheer expense of the procedure, exposure to radionuclides, and limited facilities render it an unlikely primary screen for AD.[12]

There exists a need for an AD diagnostic for detection of the disease prior to any cognitive decline. Current focus is on technologies that can detect biomarkers located elsewhere in the body. The retina is both developmentally and anatomically, a part of the CNS. It can easily be accessed for imaging in vivo by a noninvasive method.[13] Visual deficiency/performance problems are a common early complaint of AD patients.[14] However, none of these deficiencies are themselves unique to AD symptomology. There is a hope that the eye might lend

Investigative Ophthalmology & Visual Science

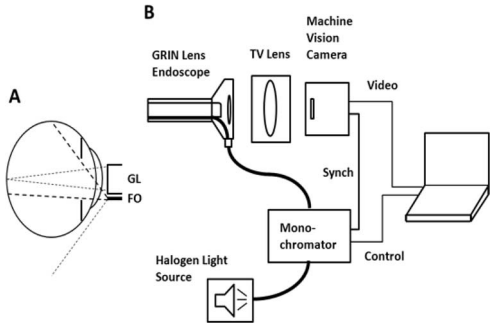

FIGURE 1. Diagram of the spectral endoscope imaging setup. (**A**) Eye in relation to receiving (GL) and emitting (FO) components of the endoscope. Section through the eye center showing recorded light rays (*short dashes*) and illuminating rays (*long dashes*). A portion of illumination is eclipsed by the pupil. The ray below the eye (*short dash*) shows the symmetric light pattern from the fiber optic. The arrangement is sensitive to both absorption and light scatter with rays entering asymmetrically over an angular spread of just under 45° while imaged light returns symmetrically about the central axis with a maximum angle of 17°. Angled illumination also reduces the pickup of light reflecting from boundaries between tissue layers, such as the internal limiting membrane of the retina. (**B**) The imaging train begins with the endoscope tip that encloses a GRIN lens. The endoscope image is refocused at the camera using a TV lens (see text). Illumination from a halogen source passes through a monochromator before entering the endoscope fiber illuminator. Image acquisition and wavelength scanning are controlled from a laptop.

biomarkers that are AD-specific and would provide an early diagnosis even before any changes happen in the brain. Retinal morphological changes have been the subject of investigation over the last decade. Changes to the retinal vasculature and optic disc,[15,16] retinal cell loss,[17,18] and thinning of the retinal nerve fiber layer (RNFL) have been observed in AD, but were nonspecific to the disease.[19] Advancement of the AD eye test from NeuroVision Imaging (Sacramento, CA, USA) into clinical trials is encouraging.[20] It utilizes retinal fluorescence photography to scan the supranuclear region of the retina for a fluorescent signature characteristic of Aβ plaques. Unfortunately, it requires administration of curcumin prior to imaging, which binds to the plaques.[21]

Recently, in an ex vivo study of transgenic Alzheimer's mice (APP/PS1),[22] we showed through hyperspectral dark-field microscopy that there exist certain optical property aberrations of the retina that are unique to AD pathology, correlated with AD progression, and occur *before* retinal plaques can be observed. Specifically, optical signals consistent with Rayleigh light scattering changes were observed in the spectrum from whole mount APP/PS1 mice retinas and their age-matched counterparts. This could be attributed to optical characteristics of retinal tissue being influenced by the assemblies of $A\beta_{1\text{-}42}$ molecules ranging from soluble colloidal form to insoluble plaques.[22] Many globular clusters that are early aggregation products of Aβ peptides are small compared with the optical wavelength and obey Rayleigh scattering theory. Since the Rayleigh scatter intensity is proportional to the inverse fourth power of wavelength,[23] buildup of small plaque precursor molecules can reduce the amount of short wavelength light obtained in reflected light recordings from the retina, resulting in a unique optical signature for early-stage AD. Rayleigh scattering is expected to be the dominant mechanism since the Aβ peptide scattering structure is much smaller than the optical wavelength.

The primary aim of the present live animal experiment was to determine if optical signals reported previously from flat-mount retinal preparations and $A\beta_{1\text{-}42}$ exposed cell culture[22] could be detected in live Alzheimer's mice, and to ascertain if the live spectral signature matches the in vitro signature. The answer to these questions will show translation of our in vitro findings into the living system and ultimately to a noninvasive method for early-stage diagnosis of Alzheimer's disease prior to cognitive decline. To carry out this work, we adapted the topical endoscopic fundus imaging (TEFI) of Paques and colleagues[24] for imaging the mouse fundus. The advantages of this method over conventional fundus photography are its low cost, good image quality, and stability over time. The method has been employed successfully for diverse studies, including color-video documentation of the retinal vascular structure,[25] panretinal imaging of ocular inflammation,[26,27] and fluorescence imaging of optogenetic probes.[28] Here we describe the new spectral imaging method and its use, and present results of optical signals produced by light-scatter changes in transgenic Alzheimer's mice with age, which may serve as a marker for buildup of amyloid aggregates in the retina.

METHODS

Mice

Wild type (B6C3F1J) and APP/PS1 double transgenic Alzheimer's mice (APPswe/PS1ΔE9) used in the present study were acquired from Jackson Laboratory (Bar Harbor, ME, USA) at the ages of 6 to 10 weeks. Eight mice were used per treatment group. All experimental procedures and animal handling were approved by the University of Minnesota Animal Care and Use Committee and were executed in accordance with the national ethics guidelines. All the animal procedures were in accordance with the ARVO Statement for the Use of Animals in Ophthalmic and Vision Research. For all experiments, animals were housed three per cage in our facility, in a controlled environment (temperature, 22°C; humidity, 50%–60%; and light from 7 AM to 7 PM); food and water were available ad libitum.

Hyperspectral Endoscopy System

Our method for spectroscopic observation in live mice is easily implemented with noninvasive fundus endoscopy. We modified the usual TEFI imaging method to enable us to record a series of images in rapid succession covering wavelengths from 480 to 705 nm. The live mouse imager (CytoViva, Inc., Auburn, AL, USA), described below, combines spatial and spectral information into a single hyperspectral image, which allows optical spectra from individual points in a sampled area to be examined. For this study, fundus images were acquired using a 5-cm gradient index (GRIN) lens otoscope with a crescent-shaped fiber illuminator on the side of the 3-mm diameter tip (type 1218 AA; Karl Storz Endoscopy, Tuttlingen, Germany). The eye receives diverging rays exiting from the side of the endoscope while light is returned from the eye by diffuse fundus reflection. The illumination path and center of the GRIN lens are separated by 1.3 mm as shown in Figure 1A, resulting in different angles for view and light input. A dual-slit scanning monochromator (model 9030; Science Tech, Inc., Toronto, Canada) was employed to obtain monochromatized illumination (15-nm bandwidth), which could be programmatically tuned between 400 and 800 nm (Fig. 1). Spectral resolution is easily changed by using slits of different width. White light from a 150-W halogen fiber-optic light source (Fiber-Lite; Dolan-Jenner Industries, Boxborough, MA, USA) was coupled to the input port of the monochromator with a 5-mm liquid light guide (Newport Corp. Irvine, CA, USA). The

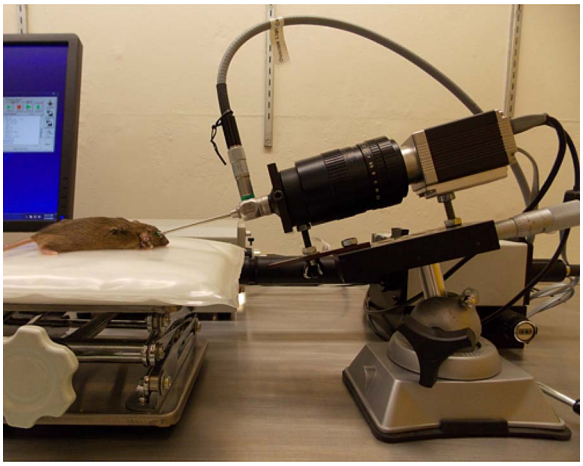

FIGURE 2. Photograph showing the endoscope recording system in relation to the mouse during imaging. Contact between the tip of the endoscope and mouse cornea is established by fine movements using a micrometer screw and with the help of a corneal gel as described in the "Imaging Procedure" section.

monochromatic light output was then coupled into the illumination optics of the endoscope using a 5-mm fluid light cable (Karl Storz Endoscopy). The endoscope was attached to a translating stage (model PT1; ThorLabs, Newton, NJ, USA), which also held a machine vision camera system (Pixelfly; PCO-Tech, Romulus, MI, USA), having 14-bit grayscale resolution in a 1392 × 1024 pixel, 2/3" image format (Fig. 2). The stage provided a 1-inch travel, controlled with a micrometer screw, which enabled gently moving the tip of the endoscope toward the corneal surface while progress was monitored with video. The endoscope image was relayed by a 50-mm f/1.4 objective lens (Nikon, Inc., Tokyo, Japan), which enabled the full field of the endoscope to be picked up by the camera. Eye safety was checked by measuring the power density (570 nm) at the endoscope tip with a digital power meter (Extech Instruments, Waltham, MA, USA). The measured reading of 160 $\mu W/cm^2$ would indicate approximately 10 μW reaching the retina, assuming a 2.8-mm dilated mouse pupil. This is considered a safe level of eye exposure based on International Electrotechnical Commission 60825 values for maximum permissible exposure.[29]

Imaging Procedure

The procedure described by Koronyo-Hamaoui et al.[21] was followed with some modifications as described. Briefly, retinas of live APP/PS1 and age-matched, wild-type (WT) mice were imaged after anesthetization with 100 mg/kg ketamine and 10 mg/kg xylazine intraperitoneally (IP) in sterile saline. A local anesthetic (proparacaine) was applied to the corneal surface prior to dilation of mouse pupils (2–3 mm diameter) with 2.5% phenylephrine hydrochloride (Bausch & Lomb, Rochester, NY, USA) and 1.0% tropicamide (Mydral; Bausch & Lomb) ophthalmic solution. Mouse eyes were covered with lubricant eye gel (GenTeal Hypromellose ophthalmic gel, 0.3%; Akorn, Lake Forest, IL, USA) for contact imaging. Care was taken to keep anesthetized animals warm throughout the procedure using warming pads. Mice were returned to their cages and monitored until the effects of the ketamine have completely subsided. These mice were sedated for imaging up to once per week using IP ketamine, if necessary.

For imaging, the anesthetized mouse was placed on a laboratory jack surface that allowed raising and lowering the animal (Fig. 2). The tip of the endoscope was brought near the cornea and coarsely aligned with the center. To aid fine alignment, illumination at 570 nm was turned on to flood the anterior eye, while video was monitored as the tip was advanced until iris reflections fell outside the view area. At this setting, a view of the posterior retina is obtained with the optic disc centered or slightly off to one side. Upon acquisition of a stable retinal image, the wavelength sequence was started to obtain a series of 16 images from 480 to 705 nm at 15-nm intervals, a process needing approximately 20 seconds. Each image was taken by the image acquisition program using an external trigger signal sent immediately after switching to the next wavelength. The image sequence was reviewed after recording and then saved as a tagged image file format image stack.

Data Analysis

Dark values were subtracted and reflection spectra were then extracted from stacks with a *z*-axis profile tool using ImageJ (http://imagej.nih.gov/ij/; provided in the public domain by the National Institutes of Health, Bethesda, MD, USA) macro language. The retinal reflection spectrum was sampled using 50 × 50 pixel averages at six positions in relatively bright regions away from nerve fibers and the large vessels. Spectra from measurement sites were averaged to give mean spectral curves for WT and Alzheimer's groups, at each age. These time-resolved reflection spectra were then normalized to unity values at 705 nm—which is outside the range where Alzheimer's-dependent spectral changes were previously observed—so that they could be compared.

Changes in light scattering and absorption were identified from optical density spectra. Optical densities in APP/PS1 mice were found using Equation 1,

$$\mathrm{OD}(\lambda) = \log_{10}[S_{\mathrm{WT}}(\lambda)/S_{\mathrm{AD}}(\lambda)] \quad (1)$$

where $S_{\mathrm{WT}}(\lambda)$ and $S_{\mathrm{AD}}(\lambda)$ represent age-matched, normalized reflection spectral amplitudes from wild-type and Alzheimer's study groups. This definition gives the relative tissue optical density from the AD group with respect to that of the age-matched WT group used as a baseline reference. The term "optical density" (OD) refers to the increment in OD between the study groups. We refer to changes in this value with age as "optical density change." Factors related to age, such as changes in melanin concentration or the number of previous imaging sessions that could affect ocular transmission, do not contribute to the OD in Equation 1. The value of our OD is zero if the AD and WT groups give the same reflected light spectrum, as would be the case if light scattering and absorption in the retina, and structures anterior, were identical in both groups. Melanin concentration would most likely average to the same value in both of our study groups, hence we would not expect Equation 1 to produce a spectrum with melanin as one of its components (Supplementary Material Fig. S1). Since retinal blood density can differ between WT and AD groups, light absorption by the blood could partially mask the light scatter spectrum. Therefore, we accounted for blood light absorption in our analysis. We used nonlinear curve fitting (Excel Solver; Microsoft Corp., Redmond, WA, USA) to fit measured optical densities of Equation 1 to a model for Rayleigh light scatter, with a term added for hemoglobin light absorption,

$$\mathrm{OD}_{\mathrm{fit}}(\lambda) = A\lambda^{-4} + B\mathrm{Hb}(\lambda) \quad (2)$$

where A and B are fitting parameters, λ^{-4} is the wavelength dependence for Rayleigh light scatter, and $\mathrm{Hb}(\lambda)$ is the hemoglobin spectrum when blood oxygen saturation is 60%,[30] which approximates the average saturation of postcap-

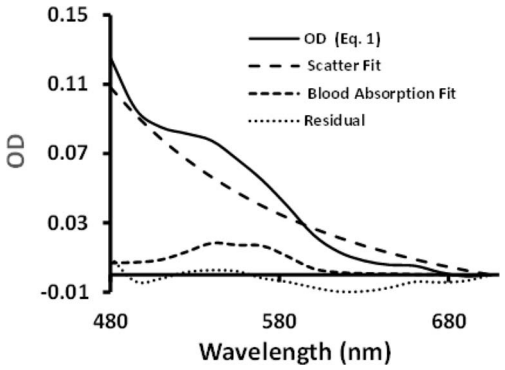

FIGURE 3. Representative curves fit to optical density spectrum from Equation 1 obtained from mice at age 7 months. Optical density spectrum (*solid line*), best fitting curves for Rayleigh scatter (*long dash*) and blood light absorption (*short dash*). The residual error is shown by the *dotted curve*. For clarity, *error bars* are omitted here and appear in Figure 6 for all time points.

illary blood. Model estimates of Rayleigh scatter and blood absorption were determined from the right-side terms of Equation 2. Figure 3 shows the relationship between measured optical density from Equation 1 and the model predictions, along with the residual curve ($OD - OD_{fit}$) for age 7 months. This method separates the contributions of light scatter and blood to allow a more accurate measure of the scatter component to use as a measure of amyloid aggregation.

Goodness-of-fit to experimental curves was determined from the coefficient of determination, R^2. Statistical significance between groups was found using an unpaired *t*-test for the difference between WT and APP/PS1 for measured optical density (Equation 1) at 480 nm, the wavelength most affected by amyloid aggregation The amyloid aggregation over time was characterized by fitting the scattering values at 480 nm to a sigmoidal function (computed by Microcal Origin 6.0; OriginLab Corp, Northampton, MA, USA). The sigmoidal growth is described by Equation 3,

$$OD_{growth}(480\,nm, t) = L\Big(1 + \exp\big(-s(t - t_0)\big)\Big) \qquad (3)$$

where L is the curve's maximum value, s gives the steepness of the curve, and t_0 is the midpoint of the curve.

The accuracy of our comparison of retinal spectra depended on the reproducibility of our recordings. It was important to insure there was no damage to the anterior eye from pressure or excessive exposure to light. Care was taken to use the minimum illumination during initial alignments and to apply illumination only over the time to complete spectral imaging. The data comparisons for calculating statistical significance were not corrected for multiple comparisons.

RESULTS

The newly developed contact-imaging system with the wavelength scanning capability was employed in the imaging of live transgenic Alzheimer's and WT mice. The performance of the contact fundus imaging with the endoscope was examined previously for color video and fluorescence imaging.[31] Our imaging experiments yielded monochromatic retinal images over a spectral range from 480 to 705 nm. The brightness and contrast of veins, arteries, nerve fibers, and choroid capillaries (Fig. 4) appear to depend on the wavelength of illumination. In blue light (510 nm, upper left, Fig. 4), nerve fibers spreading from the optic disc strongly reflect light. In green light (555 nm, upper right, Fig. 4) where

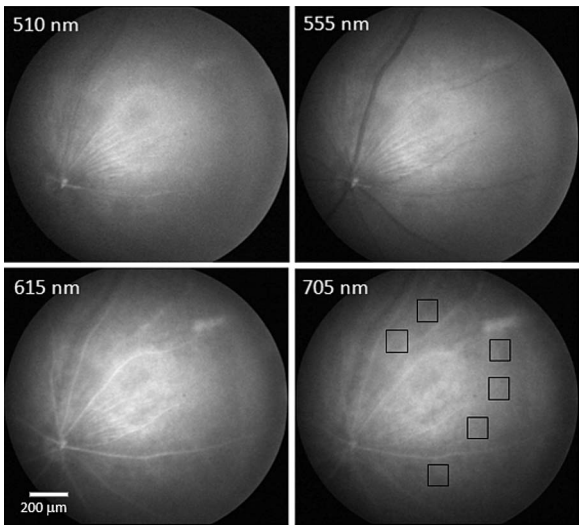

FIGURE 4. Monochromatic images from WT B6c3F1J mouse retina. *Upper left*: 510 nm (*blue light*) nerve fibers (*center*) and reflections from vessel below the fibers are bright. *Upper right*: 555 nm (*green light*), large vessels appear dark. Nerve fibers appear in *center* as bright. Veins are darker than arteries due to relatively greater absorbance of deoxyhemoglobin. *Lower left*: 615 nm (*red light*), arteries and veins both show brightly and nerve fibers are still visible. *Lower right*: 705 nm (near infrared), vessels and fibers lose brightness and deeper choroidal capillaries near center are in sharper focus. *Boxes* show locations typical of amyloid measurement areas.

hemoglobin light absorption is strong, retinal blood vessels appear dark against the fundus background, the veins being darker than the arteries due to their relatively higher content of deoxyhemoglobin. The spectral image also shows a reversal in the vessel contrast, from darker to brighter, between green (555 nm) to red (615 nm) wavelengths. In red and near infrared light (615 and 705 nm, lower left and right), both vessel types now appear bright against the background. These changes result from the absorption and scattering properties of the blood column and from specular reflections at vessel center lines. In the brown mouse, image details were largely dependent upon the wavelength: below 600 nm, image contrast was from retinal structures; while above 600 nm where melanin absorption is weaker, the retinal features were less pronounced. In nonpigmented white mice, the choroidal structures were seen across the spectrum (Supplementary Material Fig. S2). These retinal images were of higher intensity than those in brown mice due to the difference in the eye pigmentation.

Figure 5 shows optical spectra obtained from human and mouse retina. For the purpose of comparison, all spectra were normalized to unity at 705 nm where the effect of light scatter is relatively small. In Figure 5A (left panel) the upper pair of spectra were recorded from human retinal whole mounts obtained postmortem from an individual diagnosed with AD (solid line, $n = 1$) and an age-matched control subject (dashed line, $n = 1$). These are mean spectra averaged over multiple areas of the retina. The retinal spectral signature from the Alzheimer's patient with confirmed AD diagnosis showed reduced spectral amplitudes at shorter wavelengths compared with those from the age-matched normal individual. The lower pair of spectra are from live APP1/PS1 mice (solid line, $n = 8$) and live WT mice (short dashed line, $n = 8$) at age 7 months. This is the time point when the difference between Alzheimer's and WT spectra reached statistical significance ($P < 0.5$). Both human and mouse spectra exhibit similar features, including a broad range of reflected wavelengths and a

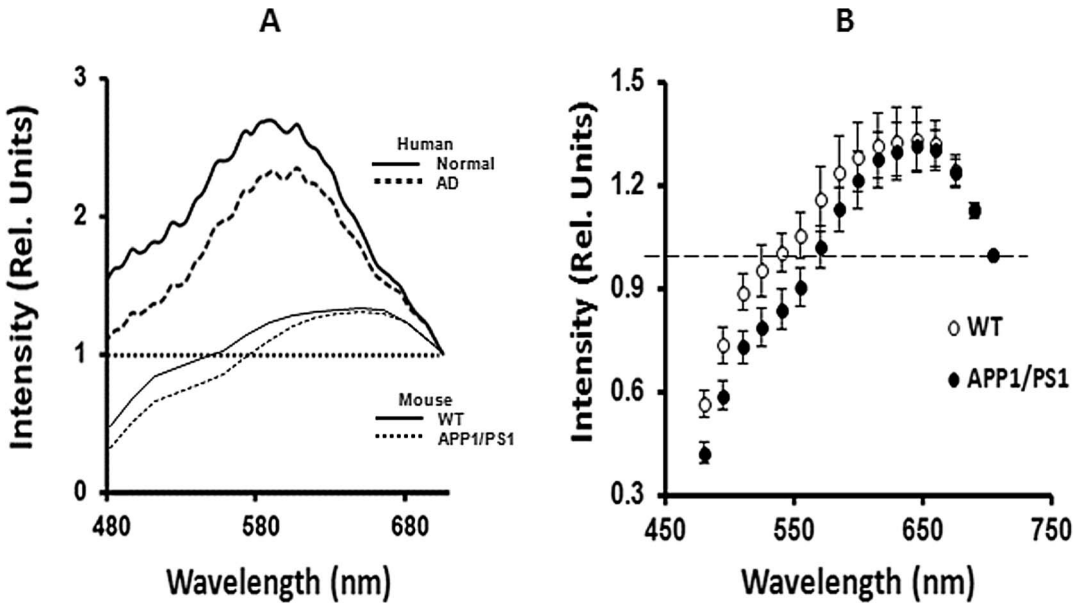

FIGURE 5. Optical spectra recorded from human and mouse retina samples. (**A**) Comparison of spectral shapes from Alzheimer's and normal retina (see the Results section). The *upper curves* show spectra from human retinal whole mounts, obtained postmortem from an individual diagnosed with AD ($n = 1$) compared with a normal subject ($n = 1$). *Lower curves* compare spectra obtained at 7 months from live APP1/PS1 mice and live WT mice ($n = 8$). (**B**) Mice spectra from (**A**) shown with standard deviations at each wavelength. At wavelengths lower than 570 nm, *error bars* from each mean spectrum do not overlap.

reduction of the Alzheimer's spectrum which strengthens going toward shorter wavelengths. This last spectral component corresponds to light loss by scatter which is modeled in Equation 2. The relative reduction in the Alzheimer's spectral amplitude was approximately the same in human (33%) and mouse (31%). Mouse spectra appear smoother because the recording was made with lower spectral resolution. Mouse spectra also reveal the presence of blood circulation by the small dip near 550 nm. We note that the human spectra were obtained using transmitted light in a dark-field microscope recording and live mouse spectra were obtained with reflected light (see the Methods section). In Figure 5B (right panel), mouse spectra from Figure 5A are shown with standard deviations at each wavelength. At wavelengths below 570 nm, the separation of means is greater than the standard deviation from each group.

Figure 6A (top panels) shows the changes in optical density (Equation 1) from live retinal images at 1-month intervals, starting at age 3 months. In earlier months, months 3 and 4, the OD curves were flat. An increase in spectral amplitude was evident at the age of 5 months, which rises progressively over the rest of the study. Beginning at 6 months, a broad peak near 550 nm was superimposed on the OD curve. This increase in OD is from a change in the volume of retinal blood, whose absorption band coincides with these wavelengths. Figure 6B (bottom panels) shows curve fits that were obtained using the Rayleigh scatter and blood absorption terms in Equation 2. The scatter component (solid line) of the optical density increased progressively over the course of this study. The presence of blood absorption (dashed line) was apparent at age 6 months and remained nearly constant after its first appearance. The appearance of the blood spectrum is consistent with an increase in retinal blood volume in the APP1/PS1 mouse relative to that of the WT mouse. Goodness-of-fits listed above each panel in Figure 6B rise to near unity at month five and remained constant for the rest of the study. Model fits at 480 nm also fell within the error of the measured OD except at 8 months, where the model prediction (0.143 OD units) was 6% below the lower error (0.153 OD units). The Table represents a summary of the above results in numerical form.

The time course of amyloid aggregation (solid bars) over the duration of this study is displayed in Figure 7, the degree of amyloid aggregation is assessed from the strength of Rayleigh light scatter at 480 nm. Rayleigh scattering is strongest at this wavelength, thus we use this value as our marker for degree of aggregation. A monotonic increase in the modelled optical density function was observed, resulting in a statistically significant difference between APP1/PS1 and WT at 7 and 8 months ($P < 0.0001$). The trend in light scatter fitted a sigmoidal growth curve (dotted line). This growth model (S parameter) predicts that by 8 months, the light scatter signal is near its maximum value of 0.148 ± 0.004 optical density units, with a midpoint of growth (t_0 parameter) at 6.18 ± 0.05 months. The amount of the optical density contributed by blood absorption (evaluated from the blood absorption model at 480 nm) is shown with open bars. There is a relatively sudden onset of increased blood volume in the APP1/PS1 retina that does not continue to rise over the remaining course of the study. An attribution of optical density changes to amyloid aggregation is supported by this numerical analysis.

DISCUSSION

We have described a method for spectroscopic analysis of retinal features in small animals using TEFI in conjunction with a spectrally tuned light source. The imaging system has sufficient spatial resolution to clearly show retinal nerve fibers and major vessels in visible through near infrared wavelengths. Our present spectral resolution of approximately 15 nm (2-mm slit width) is appropriate for the broadband light scattering signal that was found previously from tissue sections with hyperspectral microscopy. A grating monochromator design was chosen since its optical bandwidth is fixed across the tunable range of wavelengths, as it also was for the microscope hyperspectral system[22] with which the current results are being compared. Since our wavelength selection is accom-

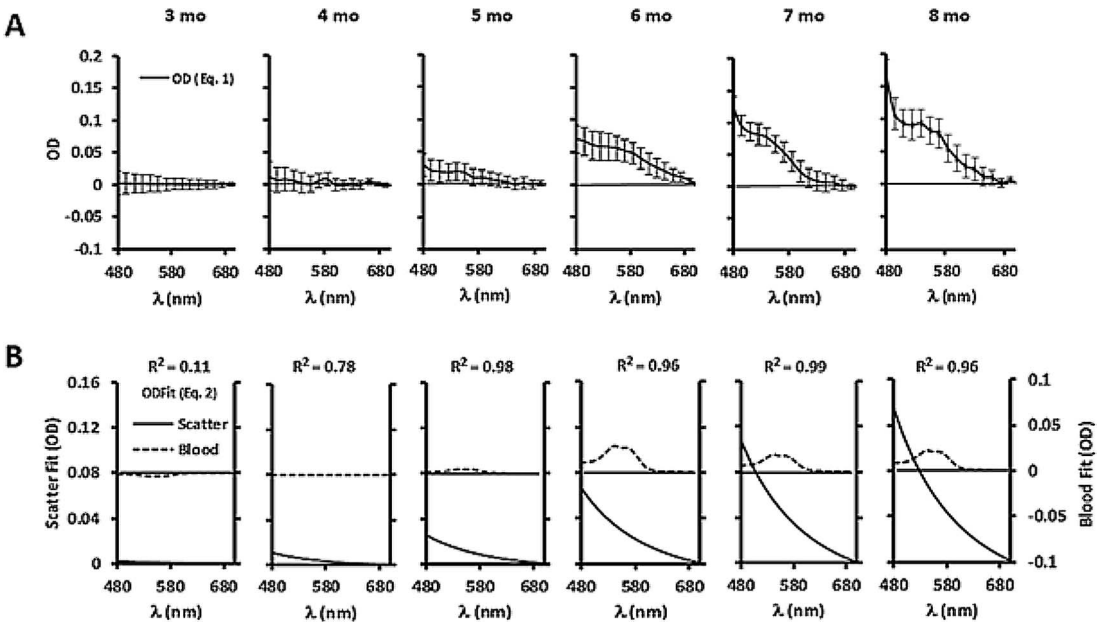

FIGURE 6. (A) Optical density curves determined by Equation 1 from consecutive study ages starting at 3 months and ending at 8 months. Curves represent the increment in optical density (OD ± SEM) of the APP/PS1 group with respect to the WT group. The curves have the form of a light scatter spectrum that increases toward shorter wavelength. At ages 6 to 8 months, curves show presence of hemoglobin light absorption near 550 nm. (**B**) Best-fitting model functions (Equation 2) for Rayleigh light scatter (*solid lines*, scale on left ordinate) and blood volume (*dashed lines*, scale on right ordinate). Goodness-of-fit is at top of each panel. Numerical values are given in the Table.

plished through the use of a grating, wavelength dispersion is linear and the optical passband is constant over wavelength. A liquid crystal tuned filter in place of the monochromator would permit faster wavelength switching, but spectral resolution would be limited to approximately 7 nm and would vary over wavelength. The present method provides a simple and inexpensive solution to spectral imaging with small animals. The 3-mm endoscope gives excellent results in white mice, where the fundal reflectance is relatively high, and in older brown mice where the dilated pupil is large enough to accept the light crescent emerging from the endoscope. We found in younger brown mice that the fundus reflectance was reduced, but was of a magnitude still usable for quantitative imaging.

Optical changes from live transgenic mice were consistent with those in $A\beta_{1\text{-}42}$ incubated cells and in retinal tissue sections obtained posthumously from Alzheimer's patients[22] suggesting a common cause. We note that our earlier in vitro recordings were made from transmitted light that was scattered from the retina with the direct illumination blocked (dark-field microscopy), while the present live recordings were of diffuse retinal reflectance obtained using an off-angle light source (TEFI endoscopy). Both types of recording have several characteristics in common: the probe light becomes diffused after undergoing multiple scattering within the tissue; only light scattered from tissue is measured; and in both cases, light intensity was reduced at shorter wavelengths in the Alzheimer's group. In our earlier dark-field recordings from retinal whole mounts, the situation is similar to dark-field microscopy in $A\beta_{1\text{-}42}$ incubated cells, where multiple scattering is required for some of the light to reach the detector. On this path toward measurement, Rayleigh scatter effects would operate (Supplementary Material Fig. S3). In the eye, light entering the retina would interact with structures of differing size and refractive index, including blood and neural cell components, and higher order Aβ oligomers. These interactions can produce Mie scattering, where light is deflected in the forward direction through small angles.[32] As this process repeats multiple times, the light paths become isotropic, causing some of the light to be returned from the retina (Supplementary Material Fig. S4 and Table S1). On the return path, Rayleigh scattering from smaller Aβ oligomers would deflect light to the side, away from the path of return, excluding it from the recorded spectrum. Since Rayleigh scattering efficiency increases as wavelength decreases, the spectrum of measured light will show a

TABLE. Fitting Parameters for OD Model

Age, mo	3	4	5	6	7	8
OD ± SE*	0.003 ± 0.018	0.012 ± 0.022	0.030 ± 0.017	0.070 ± 0.021	0.125 ± 0.016	0.169 ± 0.016
Scatter fit†	0.0025	0.016	0.0257	0.0670	0.1082	0.1346
Blood volume fit‡	−0.0015	−0.0002	0.0018	0.0109	0.0069	0.0085
A§	0.0174	0.0719	0.1737	0.4532	0.7319	0.9101
B§	−0.0408	−0.0061	0.0501	0.2953	0.1871	0.2315
P¶	0.887	0.287	0.102	0.137	1.54E-06	7.29E-06

* Optical density at 480 nm calculated from Equation 1.
† Rayleigh light scatter model is the 1st term of Equation 2: A (480 nm)$^{-4}$ (10^{10}). Model adjusted for same scale as measured OD.
‡ Blood volume model based on light absorption is the 2nd term of Equation 2: $B\text{Hb}_{60\%\text{SAT}}$ (480 nm). Hemoglobin scaled to give 0.1 OD at 540 nm.
§ Fitting parameters from Equation 2.
¶ Student's *t*-test: two tails assuming unequal variances in sample.

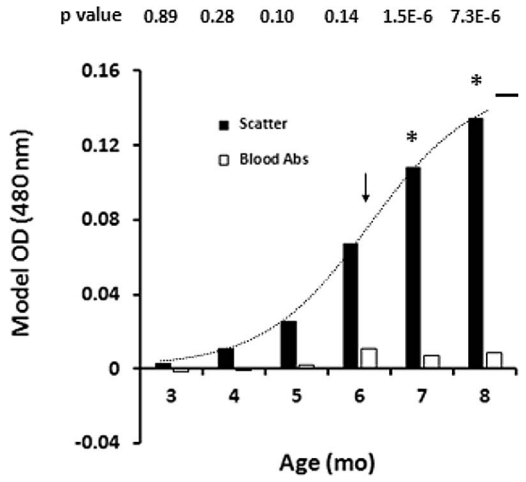

FIGURE 7. Progression of amyloid aggregation in APP/PS1 mice from age 3 to 8 months as measured by the OD value of light scatter (Equation 2, scatter fit) at 480 nm (*solid bars*, see the Methods section). *Asterisks* denote significant changes between WT and AD groups ($P < 0.0001$). The *dotted curve* shows a sigmoidal growth curve that was fit to scatter time points. The predicted midpoint in growth occurs at the *downward arrow* and maximum growth is shown by the *straight dotted line* (see the Results section). *Open bars* show the relative changes in retinal blood volume in the AD group over time at the same scale. Values of *P* are shown above the bars.

progressive loss of intensity toward shorter wavelengths. A buildup of amyloid aggregations products could thus result in the changes obtained over time in the Alzheimer's mouse. We cannot prove that the spectral changes observed in live recordings originated in a single retinal layer; however, similarity between in vitro and live signals suggests that they have a common source and the geometry suggests the inner retina contributes to the signal.

We have employed a model for Rayleigh light scatter to describe in part the measured optical density of the retina. We do not imply that the optical signature is from Raleigh scattering alone; Mie scattering phenomenon are no doubt involved. But only the large deflections produced by Rayleigh scatter and the particular wavelength dependence of this effect can explain our result. We note that the magnitude of our fitting parameter for Rayleigh scatter (*A* in Equation 2) increased monotonically with the age of the mice. The amyloid aggregation plot in Figure 7 provides target values for the optical density changes, based on the scatter model, that are associated with the aggregation process. Alternatively, the value of the Rayleigh fitting parameter, or area under the OD curve, could serve as a monitor of early-stage disease progression. A sigmoidal shape for the growth curve of Figure 7 suggests that rates of accumulation of Aβ-aggregates begin to slow after 6 months, as would be expected as smaller aggregates form into higher order Aβ oligomers and insoluble plaques without Rayleigh scatter properties. This behavior was first observed by using SH-SY5Y cells exposed to $A\beta_{1\text{-}42}$ peptide, where light extinction first increased to a maximum value and then began reducing to initial value.[22]

We note that over the course of this study the light scatter changes increased monotonically, becoming more obvious after 5 months, while APP/PS1 mouse blood volume increased abruptly after light scattering changes were in progress. We thus feel confident that the predominant origin of scatter is not from capillary blood. The ex vivo and live imaging outcomes, taken together, suggest that early stages of Aβ peptide aggregation can be detected from retinal light-scatter changes, without the addition of fluorescent labels. Techniques with demonstrated promise in measurement of the RNFL and topography changes, such as optical coherence tomography[33] and retinal fluorescence lifetime imaging,[34] could potentially be excellent complimentary methods to retinal hyperspectral imaging for yielding physical parameters of the optical feature being characterized. However, if a test for AD is to be based on light scatter profiles, aging effects that could impact ophthalmic imaging such as yellowing of the lens[35] and lens thickness[36,37] should be considered. In drug development testing, age-related increases in lens scatter can most likely be compensated using age-matched groups in comparative studies. On the other hand, clinical early detection must work in individuals; young and old may be at risk for AD. There may be an age-adjusted threshold that takes into account shifts in optical properties of lens and other, which would make it possible to determine if there is an increased risk for AD from retinal light scatter results. Such tests may need to be repeated. In this case, test intervals would likely be short compared to time courses of age-related changes.

Our observation that the retinal blood volume is elevated during disease progression is contrary to reports in the literature for early AD.[15] The following factors are at play: we have employed ketamine/xylazine as the anesthetic; plausibly, reflex/feedback vasodilation (localized) could be a contributor. Our mouse studies are conducted at ages earlier than those that correspond to "early AD" in humans, implying that retinal blood-flow may be elevated and then depleted as a function of disease progression. This second factor could represent early inflammation response followed by reduced demand for blood flow as neuronal activity declines. Finally, we also have not directly measured blood-flow in contrast with the reported study.

Over the past few years, consensus on the molecular players in AD symptomology has begun to coalesce around Aβ-aggregates of an order between individual strands and plaques. It has now been shown at a molecular level that *soluble* Aβ-aggregates such as globulomers and pore-forming hollow rods interact specifically with neuronal cell-membrane components. While pore-forming rods compromise membrane integrity, allowing for general disruption of homeostasis, globulomers strongly agonize N-methyl-D-aspartate receptors. The latter directly causes psychiatric changes as well as intense oxidative stress in the cytoplasm that, over time, will lead to neuronal cell-death. In this respect, we believe that the technique disclosed in this report is the first to show ability to exploit the unique optical properties of suspended particles in the size-range of ~50 to 500 nm (Rayleigh scattering itself and various magnitudes and directionalities of Mie scattering phenomenon). This size-range coincides with that of those Aβ aggregation orders that are not just increasingly accepted, but shown on a molecular level to be some of the pathologic entities that cause the symptoms as well as underlying the progressive neuronal damage of AD.

Conclusions and Future Direction

This is the first instance of the detection of early Alzheimer's disease in a live Alzheimer's mouse using hyperspectral imagery and without the use of an extraneous agent. The technique described herein is noninvasive. In view of the possibility that light scattering signals could be used to detect and monitor early stages of AD in patients, one must consider eye safety and effects of aging. We were able to measure the signals in live mice using safe levels of light exposure over tens of seconds. It is anticipated that similar exposure durations would be used to examination light scattering changes in patients. Timely diagnosis of AD is paramount for proper

treatment and evaluation of the latter's efficacy. We expect this technology to prove suitable for translation into a human diagnostic tool. Such developmental efforts are underway.

Acknowledgments

Supported by the Center for Drug Design endowment to the University of Minnesota.

Disclosure: **S.S. More**, P; **J.M. Beach**, None; **R. Vince**, P

References

1. Alzheimer's's Association. 2016 Alzheimer's's disease facts and figures. Available at: http://www.alz.org/facts/overview.asp. Accessed June 2, 2015.
2. Armstrong RA. Plaques and tangles and the pathogenesis of Alzheimer's's disease. *Folia Neuropathol*. 2006;44:1–11.
3. Huang Y, Mucke L. Alzheimer's mechanisms and therapeutic strategies. *Cell*. 2012;148:1204–1222.
4. Kung HF, Choi SR, Qu W, Zhang W, Skovronsky D. 18F stilbenes and styrylpyridines for PET imaging of A beta plaques in Alzheimer's's disease: a miniperspective. *J Med Chem*. 2010; 53:933–941.
5. Corder EH, Saunders AM, Strittmatter WJ, et al. Gene dose of apolipoprotein E type 4 allele and the risk of Alzheimer's's disease in late onset families. *Science*. 1993;261:921–923.
6. Zekanowski C, Styczyńska M, Pepłońska B, et al. Mutations in presenilin 1, presenilin 2 and amyloid precursor protein genes in patients with early-onset Alzheimer's's disease in Poland. *Exp Neurol*. 2003;184:991–996.
7. Doecke JD, Laws SM, Faux NG, et al. Blood-based protein biomarkers for diagnosis of Alzheimer's disease. *Arch Neurol*. 2012;69:1318–1325.
8. Sunderland T, Linker G, Mirza N, et al. Decreased beta-amyloid1-42 and increased tau levels in cerebrospinal fluid of patients with Alzheimer's disease. *JAMA*. 2003;289:2094–2103.
9. Blennow K, Hampel H, Weiner M, Zetterberg H. Cerebrospinal fluid and plasma biomarkers in Alzheimer's disease. *Nat Rev Neurol*. 2010;6:131–144.
10. Morris JC, Roe CM, Grant EA, et al. Pittsburgh compound B imaging and prediction of progression from cognitive normality to symptomatic Alzheimer's disease. *Arch Neurol*. 2009;66: 1469–1475.
11. Thal LJ, Kantarci K, Reiman EM, et al. The role of biomarkers in clinical trials for Alzheimer's disease. *Alzheimer's Dis Assoc Disord*. 2006;20:6–15.
12. Anoop A, Singh PK, Jacob RS, Maji SK. CSF biomarkers for Alzheimer's's disease diagnosis. *Int J Alzheimer'ss Dis*. 2010; 2010:606802.
13. Frost S, Kanagasingam Y, Sohrabi H, et al. Retinal vascular biomarkers for early detection and monitoring of Alzheimer's's disease. *Transl Psychiatry*. 2013;3:e233.
14. Armstrong RA. Alzheimer's's disease and the eye. *J Optom*. 2009;2:103–111.
15. Berisha F, Feke GT, Trempe CL, McMeel JW, Schepens CL. Retinal abnormalities in early Alzheimer's's disease. *Invest Ophthalmol Vis Sci*. 2007;48:2285–2289.
16. Tsai CS, Ritch R, Schwartz B, et al. Optic nerve head and nerve fiber layer in Alzheimer's's disease. *Arch Ophthalmol*. 1991; 109:199–204.
17. Blanks JC, Hinton DR, Sadun AA, Miller CA. Retinal ganglion cell degeneration in Alzheimer's's disease. *Brain Res*. 1989; 501:364–372.
18. Blanks JC, Schmidt SY, Torigoe Y, Porrello KV, Hinton DR, Blanks RH. Retinal pathology in Alzheimer's's disease. II. Regional neuron loss and glial changes in GCL. *Neurobiol Aging*. 1996;17:385–395.
19. Paquet C, Boissonnot M, Roger F, Dighiero P, Gil R, Hugon J. Abnormal retinal thickness in patients with mild cognitive impairment and Alzheimer's's disease. *Neurosci Lett*. 2007; 420:97–99.
20. *Retinal amyloid fluorescence imaging predicts cerebral amyloid burden and Alzheimer's disease*. Copenhagen, Denmark, July 12–17, 2014. Alzheimer's Association International Conference, 2014.
21. Koronyo-Hamaoui M, Koronyo Y, Ljubimov AV, et al. Identification of amyloid plaques in retinas from Alzheimer's's patients and noninvasive in vivo optical imaging of retinal plaques in a mouse model. *Neuroimage*. 2011;54:S204–S217.
22. More SS, Vince, R. Hyperspectral imaging signatures detect amyloidopathy in Alzheimer's's mouse retina well before onset of cognitive decline. *ACS Chem Neurosci*. 2015;6:306–315.
23. Jacques SL. Optical properties of biological tissues: a review. *Phys Med Biol*. 2013;58:R37–R61.
24. Paques M, Guyomard JL, Simonutti M, et al. Panretinal, high-resolution color photography of the mouse fundus. *Invest Ophthalmol Vis Sci*. 2007;48:2769–2774.
25. Guyomard JL, Rosolen SG, Paques M, et al. A low-cost and simple imaging technique of the anterior and posterior segments: eye fundus, ciliary bodies, iridocorneal angle. *Invest Ophthalmol Vis Sci*. 2008;49:5168–5174.
26. Copland DA, Wertheim MS, Armitage JW, Nicholson LB, Raveney BJE, Dick AD. The clinical time-course of experimental autoimmune uveoretinitis using topical endoscopic fundal imaging with histologic and cellular infiltrate correlation. *Invest Ophthalmol Vis Sci*. 2008;49:5458–5465.
27. Chu CJ, Herrmann P, Carvalho LS, et al. Assessment and in vivo scoring of murine experimental autoimmune uveoretinitis using optical coherence tomography. *PLoS One*. 2013;8: e63002.
28. Schejter A, Tsur L, Farah N, Reutsky-Gefen I, Falick Y, Shoham S. Cellular resolution panretinal imaging of optogenetic probes using a simple funduscope. *Trans Vis Sci Tech*. 2012;1(2):4.
29. Focus Technologies, LLC. Maximum permissible exposure. Available at: http://www.focustechnologies.us/wp-content/uploads/2013/12/Laser-safety-Wikipedia-Maximum-Exposure-Limits.pdf. Accessed May 31, 2016.
30. Prahl S. Optical absorption of hemoglobin. Available at: http://omlc.ogi.edu/spectra/hemoglobin/index.html. Accessed May 2, 2016.
31. Quinten M, Stier J. Absorption of scattered light in colloidal systems of aggregated particles colloid. *Polym Sci*. 1995;273: 233–241.
32. Kalashnikov M, Choi W, Hunter M, Yu CC, Dasari RR, Feld MS. Assessing the contribution of cell body and intracellular organelles to the backward light scattering. *Opt Express*. 2012; 20:816–826.
33. Drexler W, Morgner U, Ghanta RK, Kartner FX, Schuman JS, Fujimoto JG. Ultrahigh-resolution ophthalmic optical coherence tomorgraphy. *Nat Med*. 2001;7:502–507.
34. Jentsch S, Schweitzer D, Schmidtke KU, et al. Retinal fluorescence lifetime imaging ophthalmoscopy measures depend on the severity of Alzheimer's's disease. *Acta Ophthalmol*. 2015;93:e241–e247.
35. Cooper GF, Robson JG. The yellow colour of the lens of man and other primates. *J Physiol*. 1969;203:411–417.
36. Mellerjo J. Light absorption and scatter in the human lens. *Vision Res*. 1971;11:124–141.
37. Pokorny J, Smith VC, Lutze M. Aging of the human lens. *Appl Opt*. 1987;26:1437–1440.